Shortwave Flux from Satellite-Measured Radiance: A Theoretical Study over Marine Boundary Layer Clouds

L. H. CHAMBERS AND B. A. WIELICKI

Atmospheric Sciences, NASA Langley Research Center, Hampton, Virginia

N. G. LOEB

Center for Atmospheric Sciences, Hampton University, Hampton, Virginia

(Manuscript received 12 March 2001, in final form 16 July 2001)

ABSTRACT

Earth radiation budget measurements, important to climate monitoring and to validating climate models, require that radiances measured by satellite instruments be converted to hemispherical flux. This paper examines that problem theoretically, using inhomogeneous cloud models constructed from Landsat scenes of marine boundary layer clouds. The spherical harmonics discrete ordinates method (SHDOM) code is applied to the model scenes to compute full two-dimensional radiation fields, which then simulate measured radiances. Inversion to flux is performed by several different methods, including plane-parallel table lookup and empirical angular distribution models with three different ways of determining scene identification, to examine error sources and relative magnitudes. Using a simple plane-parallel table lookup results in unacceptably large flux bias errors of 11%–60%, depending on the orbital viewing geometry. This bias can be substantially reduced, to no more than 6%, by using empirical angular distribution models. Further improvement, to no more than 2% flux bias error, is obtained if known biases in optical-depth retrievals are taken into account when building the angular models. Last, the bias can be further reduced to a fraction of a percent using scene identification based on multiple views of the same area. There are limits, however, to the reduction in the instantaneous error with this approach. Trends in the flux error are also identified, in particular an equator-to-pole trend in the flux bias. Given the importance of satellite measurements for determining heat transport from equator to pole, this consistent bias should be kept in mind, and efforts should be made to reduce it in the future.

1. Introduction

Determination of radiative energy fluxes emitted and reflected by the earth is a challenge for earth-observing satellite instruments, because they generally can measure energy only in a limited solid angle. The conversion from a radiance measurement to a hemispherical flux requires some model of the angular distribution of radiation. Four standard approaches exist. The simplest is to assume a plane-parallel scene and to use one-dimensional radiative transfer models to infer the flux. A more empirical approach was employed in the Earth Radiation Budget Experiment (ERBE; Barkstrom 1984), in which a maximum-likelihood estimator (MLE; Wielicki and Green 1989) algorithm based only on the measured shortwave and longwave radiances is used to classify scenes into 12 categories. Empirical angular distribution models (ADMs) are then applied to convert radiance to flux. The more recently launched Clouds and the Earth's Radiant Energy System (CERES) instruments extend this approach by using data from coincident imager instruments [Visible Infrared Scanner (VIRS) on the *Tropical Rainfall Measuring Mission* (*TRMM*) spacecraft or Moderate-Resolution Imaging Spectroradiometer (MODIS) on the *Terra* spacecraft]. A much greater number of scene categories can thus be identified, and empirical ADMs can be built for each (Wielicki et al. 1996). Other instruments, such as the Polarization and Directionality of Earth Reflectances (POLDER; Deschamps et al. 1994) and Multiangle Imaging Spectroradiometer (MISR; Diner et al. 1998), use multiple views of the same target to improve the characterization of the angular distribution of radiation.

Error goals for CERES and ERBE are summarized in Table 4 of Wielicki et al. (1995a). To date, the stability of the CERES instrument on orbit, monitored with an onboard calibration source traceable to the 1990 International Temperature Scale standard, has been excellent: a few tenths of a percent (Priestley et al. 2000). Thus, errors in the radiance measurements themselves are very small. Conversion to flux remains an issue, however.

This study examines error sources in three of the

Corresponding author address: Lin H. Chambers, Radiation and Aerosols Branch, MS 420, NASA Langley Research Center, Hampton, VA 23681-2199.
E-mail: l.h.chambers@larc.nasa.gov

above approaches for obtaining shortwave flux from radiance measurements (not MLE, which requires longwave information) but does not precisely duplicate any actual instrument processing. The theoretical calculations are monochromatic and assume a perfect spectral response; a single channel (visible) threshold is used to detect clouds. The advantages of this simulation approach are that a realistic cloud definition can be made at the Landsat spatial scale (28.5 m), that the ''true'' flux is known from the radiative transfer calculation, and that explicit three-dimensional (3D) cloud effects are known.

Section 2 describes the tools and data used for this study. Section 3 explains the simulation of the retrieval process. Section 4 summarizes the results, which are further discussed in section 5.

2. Data and tools

a. Landsat scenes

The Landsat scenes used were chosen by examination (Wielicki and Parker 1992) to select a wide range of cloud fraction, cell size, cell horizontal aspect ratio, and open and closed cellular convection cases. Thus, the intent of the dataset is not to represent the long-term conditions of any particular region of the earth but rather to cover reasonably the range of oceanic boundary layer cloud variability that might be observed from space. Samples of trade cumulus, broken stratocumulus, and overcast stratus are included. Landsat thermal infrared data for clear and optically thick portions of the cloud fields were used to confirm that the difference between clear-sky temperature and cloud temperature was typical of that expected for boundary layer cloud fields ($<\sim$20 K, corresponding to about 3-km cloud-top height). Cases not included in this dataset are boundary layer clouds over land, snow, or ice, or any boundary layer cloud cases that showed evidence of mid- or high-level clouds. The majority of the cases found were subtropical oceanic boundary layer cloud.

Cloud fields that are reasonably statistically homogeneous over the analyzed region were required. That is, areas with large qualitative changes in cloud cell size, orientation, or cover were avoided. The practical result of this last requirement was that the 180-km Landsat scene was typically too large to meet the qualitative statistical homogeneity criteria. Therefore, a smaller analysis area was chosen (58.4 km, or 2048 by 2048 pixels). This smaller analysis region allowed a marked improvement in the statistical homogeneity of the cloud fields.

As a result of the selection process, 52 Landsat scenes of marine boundary layer clouds were available for this study. Scenes 1–45 are described in the work of Harshvardhan et al. (1994). Of those, seven were rejected because more than 10% of the pixels were saturated in reflectance (scenes 1, 13, 20, 25, 26, 27, and 42). Additional scenes studied in this paper are summarized in Table 1 of Chambers et al. (1997). For the 45 scenes used here, the mean saturation is 1.1%, with a minimum of zero saturation and a maximum of almost 7%. A few representative scenes of each type are reproduced in Plate 1 of Chambers et al. (1997). Again, these cases do not represent the frequency of occurrence for any particular location.

The Landsat data are converted from digital counts to spectral radiance I and then to an equivalent Lambertian reflectance $R = \pi I/F_s(t)\cos\theta_0$, as described by Wielicki and Welch (1986). Here, $F_s(t)$ is the incoming spectral solar flux corrected for Earth–Sun distance and θ_0 is the corresponding solar zenith angle. The clear-sky reflectance and cloud threshold are then determined and are used to separate the Landsat image into clear and cloudy pixels as for the reference cloud-cover determination in Wielicki and Parker (1992). For each cloudy flagged pixel, the Landsat 0.83-μm nadir reflectance (the band with the best dynamic range for clouds) is converted to an estimate of cloud optical depth τ. This conversion is done by first removing the small component of ocean surface reflection and then assuming that each Landsat cloudy pixel can be modeled as a plane-parallel cloud (independent pixel approximation assumption; Cahalan et al. 1994). Conversion of reflectance to τ is based on interpolation in a lookup table derived using the discrete-ordinate radiative transfer multiple-scattering model of Tsay et al. (1990) for monochromatic radiation at 0.83 μm. A 10-μm effective radius r_e is used in this retrieval. At this wavelength, the sensitivity to particle size is negligible unless r_e is less than 5 μm (Watts et al. 1998). The retrieved values of optical depth can range from as small as 0.082 to a maximum value of 100; the latter is due to the relative insensitivity of reflectance to optical depth for larger values of τ. A very small portion (less than 0.1%) of the Landsat data in this study exceeded this upper limit. The maximum optical-depth saturation for any given scene is less than 2%; for most scenes it is zero. Areas with optical-depth saturation are avoided in the subsampling process described in the next section.

b. Cloud model

To keep the computational burden tractable for the radiative transfer calculation, the Landsat scenes must be subsampled into a limited number of strips. Full 3D calculations are still too computationally expensive for such a study and have been shown (Chambers 1997) to be similar qualitatively to the two-dimensional (2D; x–z) results. In this study, cloud samples consist of 10-km-long strips and are selected by sampling the widest possible variability, in terms of cloud fraction A_c and mean cloud optical depth, from the 45 Landsat scenes. This results in 341 cloud samples, which are distributed in terms of cloud fraction and optical depth as shown in Table 1. (Although none of the samples had an av-

TABLE 1. Distribution of cloud samples in terms of true cloud fraction A_c and cloud optical depth τ_c.

	A_c					
τ_c	0.–0.01	0.01–0.25	0.25–0.5	0.5–0.75	0.75–0.99	0.99–1.0
0–2.5	20	20	19	21	20	8
2.5–6	0	20	20	21	22	20
6–10	0	7	9	12	21	20
10–18	0	2	2	3	11	20
18–40	0	1	1	0	2	19
>40	0	0	0	0	0	0

erage optical depth above 40, pixel optical depths up to 100 are included.) The goal was to obtain about 20 samples in each bin. Bins that are underfilled indicate rarer cloud property combinations. [As has been noted before in Chambers et al. (1997), there do not appear to be many oceanic boundary layer clouds in nature that are both very thick and have a small cloud fraction.]

The generation of realistic 2D inhomogeneous cloud fields from these samples proceeds as follows: the variation of microphysical quantities in the vertical direction is generated by introducing a particle size variation as a function of height within the cloud. Based on thermodynamic principles (e.g., Rogers and Yau 1989; Considine et al. 1997) a linear variation of liquid water content with height is used. Following the method of Martin et al. (1994), the effective particle radius is

$$r_e = \left[\frac{3L(z)}{4\pi\rho_w k N_{\mathrm{TOT}}}\right]^{1/3}, \tag{1}$$

where $L(z) = Az$ is the mass of liquid water per unit volume of air and is assumed to vary linearly as a function of height z above cloud base. The density of liquid water is denoted ρ_w, and N_{TOT} is the total droplet concentration. The parameter k is set to 1 in each cloud column under the assumption of adiabatic ascent from local cloud base [G. Considine 1996, personal communication; note that other values proposed for k in Martin et al. (1994) would cause at most a 10% increase in r_e, which is insignificant in this study]. Here, N_{TOT} is set to 150 cm^{-3}, which turns out to be a bit high but not outside the range for marine boundary layer clouds (Miles et al. 2000).

Assuming the extinction efficiency factor is equal to 2, because the cloud drops are large when compared with the wavelength, the optical depth can be estimated (Nakajima and King 1990) from

$$\tau \approx \frac{3}{2\rho_w}\int_0^{\Delta z}\frac{L(z')}{r_e(z')}\,dz'. \tag{2}$$

Substituting $L = Az$ and Eq. (1) for r_e gives

$$\tau \approx \frac{3}{10}\left(\frac{3A}{\rho_w}\right)^{2/3}(4\pi N_{\mathrm{TOT}})^{1/3}\Delta z^{5/3}, \tag{3}$$

where Δz is the cloud thickness in meters. The constant A that describes the liquid water content variation can be calculated from thermodynamics. A value for A of 0.0021 g m^{-4} is found to be consistent with an empirical relation for Δz from Minnis et al. (1992), remarkably close to the value used by Austin et al. (1995). Given τ from the Landsat scene, Eq. (3) can be used to set the cloud geometric thickness Δz. The extinction is now also a function of height within the cloud and can be calculated from

$$\beta_e(z) = 2\pi(0.001)[r_e(z)]^2 N_{\mathrm{TOT}}. \tag{4}$$

With N_{TOT} in inverse centimeters cubed and r_e in micrometers, this gives β_e in inverse kilometers.

Radiative properties of the cloud particles at the 0.83-μm wavelength of this study assume conservative scattering. A Mie calculation is used to compute the phase function for lognormal distributions of cloud particles with a range of effective radius. Gas absorption is not considered, because the main focus of this study is on the effects of cloud inhomogeneity.

The macrophysical features of the cloud sample are set to match known features of cloud fields. A distribution with 10% of the cloud-thickness variability in the cloud top was used initially (i.e., 0.1 of cloud thickness above and 0.9 below a specified height in the atmosphere). This distribution was based on theoretical calculations by G. Considine (1996, personal communication) and an expectation that these marine boundary layer clouds are inversion capped and, therefore, have fairly uniform tops (''capped model''). Statistics obtained from the Lidar In-Space Technology Experiment (Loeb et al. 1998) were used to establish another distribution of cloud-top bumps in which 80% of the cloud-thickness variability is in the cloud top (i.e., 0.8 of cloud thickness above and 0.2 below a specified level in the atmosphere; ''bumpy model''). In the former case, cloud-top bumps are on the order of 30 m and less (optical depth of bumps is less than 1); in the latter they are up to 100 m for overcast clouds and up to 300 m for broken clouds (bump optical depths ~2–10). Analysis of 3 months of cloud radar data from the Atmospheric Radiation Measurement Program site at Nauru in the tropical western Pacific suggests that the bumpy model is a better representation of the measured cloud fields. There remains a question, however, as to whether the Nauru data are representative of the Tropics as a

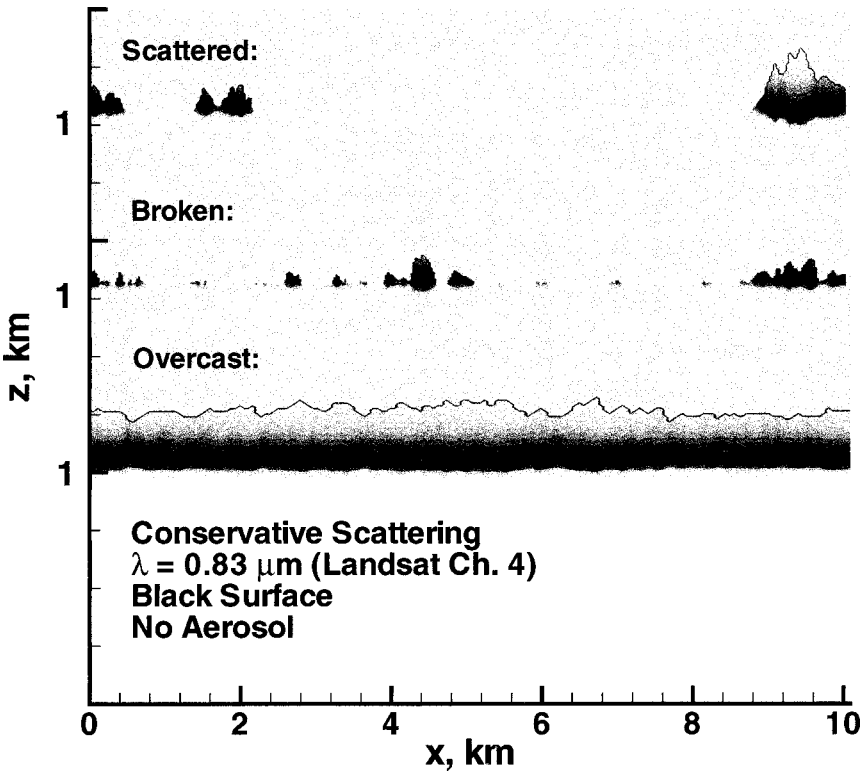

FIG. 1. Sample 2D cloud fields showing the magnitude of cloud-top variability and the variation of extinction within the cloud. Scattered, broken, and overcast cloud-field samples are shown for the bumpy model.

whole or whether there is a significant island effect (Nordeen et al. 2001).

All the cloud properties are discretized onto a spatial grid for input to the spherical harmonics discrete ordinates method (SHDOM) radiative transfer code. The grid interval in the horizontal direction x is that of the Landsat scene (generally 28.5 m; except for a few scenes from the older Landsat sensor with 57-m pixels), and the vertical grid spacing is set so the maximum vertical optical depth in any grid cell is less than 1. Sample scattered, broken, and overcast 2D cloud fields from the bumpy model are shown in Fig. 1. Note that this approach to generating 2D cloud profiles results in clouds with no internal holes.

c. SHDOM code

The radiative transfer (RT) model used in this study is the SHDOM method described in Evans (1998). In brief, it uses both spherical harmonics and discrete ordinates to represent the radiance field during different parts of the solution algorithm. The spherical harmonics are employed for efficiently computing the source function, including the scattering integral. The discrete ordinates are used to integrate the radiative transfer equation through the spatial grid. The solution method is simply to iterate between the source function and radiance field, akin to a successive order of scattering approach. For the results calculated here, the number of discrete ordinate directions is set to $N_\mu = 12$ and $N_\phi = 24$. These choices were based on an angular resolution sensitivity study to provide good accuracy at all angles of interest.

For each of the 341 scan-line samples selected for this study, RT solutions at 0.83-μm wavelength are obtained at 10 solar zenith angles (0°, 5°, 15°, 25°, 35°, 45°, 55°, 65°, 75°, and 85°) assuming 2D radiative transfer (no net transport of radiation in the y direction). Results obtained are the flux at the top of the atmosphere (TOA) as a function of x and the radiance at the TOA as a function of x for 109 viewing angles ($\theta = 0°$, and all combinations of $\theta = 5°$, 15°, 25°, 35°, 45°, 55°, 65°, 75°, and 85° and $\phi = 0°$, 5°, 20°, 40°, 60°, 80°, 100°, 120°, 140°, 160°, 175°, and 180°). This calculation required approximately 3 months of CPU time on an R10000 computer processor chip.

3. Retrieval process: Strategies

To assess methods to convert satellite-measured radiances to flux, the radiances computed by the SHDOM model are treated as if they are radiances measured from an instrument in Earth orbit (albeit an instrument with a perfect, very narrowband spectral response). The pri-

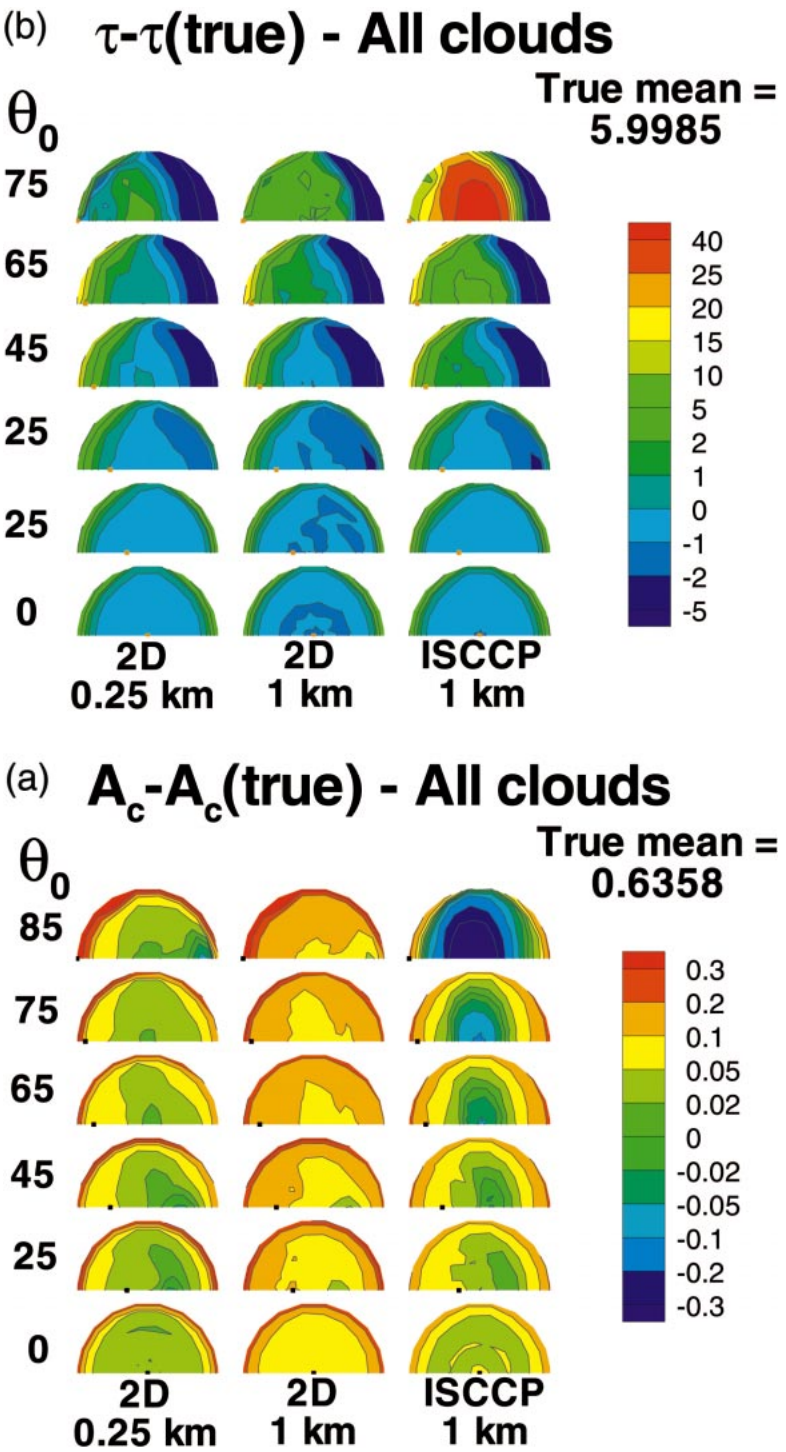

FIG. 2. (a) Error in retrieved cloud fraction for various imager pixel sizes, cloud detection thresholds, and sun angles, for all cloud samples. Viewing zenith and relative azimuth angle are represented in half-polar plots in which nadir view is at the center of the semicircle, forward-scatter is to the right and backscatter is to the left. The small black square marks the solar zenith angle. All retrievals are done by a 0.83-μm reflectance-threshold test on the computed 2D reflectance field. (b) Error in retrieved optical depth for various imager pixel sizes, cloud detection thresholds, and sun angles, for all cloud samples. All retrievals are done by a plane-parallel lookup table from the computed 2D reflectance field for pixels labeled as cloudy. Pixel-scale optical depths for cloudy pixels are then logarithmically averaged to obtain a mean value for the sample.

mary retrieval process simulated here is that used with the CERES data. For comparison, results are also computed using an algorithm similar to that used in the International Satellite Cloud Climatology Project (ISCCP; Rossow and Garder 1993) and for instruments such as MISR and POLDER that provide multiple views of a scene from different angles. There are two principal differences between the CERES and ISCCP approaches: 1) different reflectance thresholds, with a different dependence on view angle, are used for the determination of clear versus cloudy pixels and 2) ISCCP does not retrieve flux. In this comparison, we use a plane-parallel model to retrieve flux given the ISCCP-retrieved cloud properties as a way to assess errors arising from the plane-parallel assumption.

a. Step 1: Imager reflectance

The computed Landsat-scale radiances I at each angle are averaged to the resolution of the field of view of the MODIS instrument: 0.25 km for full scale and 1 km for reduced-resolution mode (the latter also approximates the 2-km footprint size of the VIRS instrument on *TRMM*). Simple averaging is done without consideration of the instrument point spread function. The radiances then are converted to imager-scale reflectance R:

$$R(\theta, \phi; \theta_0) = \pi I(\theta, \phi; \theta_0)/(\mu_0 F_s), \quad (5)$$

where F_s is the incoming solar flux at 0.83 μm and μ_0 is the cosine of the solar zenith angle.

b. Step 2a: Property retrieval and scene identification

The imager-scale reflectances are used to retrieve scene properties at each view and solar zenith angle for each sample. First, cloud–clear radiance thresholds $I_{\rm clr} + \sigma(\theta, \phi, \theta_0)$ are applied to decide whether an imager pixel is clear or cloudy. The variability in the clear-sky radiance σ is that from the CERES processing algorithm for ocean surfaces (Wielicki et al. 1995b); for the ISCCP threshold it is $3\%/\mu_0$. (State-of-the-art algorithms use a three-channel cloud mask, but most boundary layer clouds are detected primarily by the shortwave threshold.) Here, $I_{\rm clr}$ comes strictly from Rayleigh scattering in the modeled atmosphere, because there is no surface reflection or aerosol in the model.

For pixels identified as cloudy, a lookup table built from plane-parallel runs of the SHDOM code is used to determine optical depth. Cloud fraction and mean (logarithmically averaged) cloud optical depth are then computed for each sample and at all angles. This computation constitutes the scene identification (scene ID). In practice, additional parameters (e.g., surface type, cloud phase, cloud height or temperature) would also be part of the scene ID. The scene ID is used to group together pixels that are presumed to have similar anisotropic behavior into an ADM and also to select the correct ADM from which to convert a measured radiance to a hemispherical flux. This approach is an empirical way to account for differences in angular patterns of radiance emanating from different scenes on the earth.

The scene ID that is retrieved depends on the viewing geometry, because of the application of a plane-parallel retrieval to 2D clouds. Figure 2a summarizes the cloud fraction errors that are incurred in this process. The different angular variation of the ISCCP thresholds versus those for CERES results in very distinct error patterns. Also of note is the bias in retrieved cloud fraction for the 1-km imager pixel size (see beam-filling discussion in section 5).

Figure 2b shows retrieval errors for cloud optical depth τ. Note the forward- versus backscatter retrieval bias that becomes more pronounced at large solar zenith angles: τ is consistently underestimated for viewing angles in the forward-scatter direction and is consistently overestimated for backscatter view angles. This does not correlate with any features in the cloud fraction retrieval but is consistent with previous findings (e.g., Loeb and Coakley 1998). Note also that there is a small negative bias in optical depth at small solar zenith angles for all but the most oblique view angles. For this parameter, there is not much effect from changing imager pixel size.

c. Step 2b: Percentile scene ID

A scene ID is also computed by a second method, based on an approach used by Loeb et al. (2000). This method attempts to account for the bias errors in the optical-depth retrieval noted above by defining percentile classes of τ rather than placing scenes in fixed τ classes. The cloud fraction is determined as before, but then the samples are stratified in each A_c and angle bin according to their relative brightness. This method groups populations consistently from different viewing geometries. For example, the brightest 5% at each angle go to form a single ADM class. The assumption, tested by the results in this paper, is that the cloud that appears brightest at one view angle is also brightest at another view angle and will thus be put in the same class. The percentile intervals used and the number of samples in each class, based on the true scene ID, are given in Table 2. Note that, for equal percentile intervals, the number of samples is about the same.

d. Step 2c: Multiple-view scene ID

As shown in Figure 2, the error in retrieved scene properties has some systematic variation with viewing geometry. If multiple views are available and the properties for each view are averaged, a much better approximation of the true scene ID may be obtained.

The MISR instrument (Diner et al. 1998) is on the *Terra* spacecraft, with nine cameras taking images at alongtrack view angles that are symmetric forward and

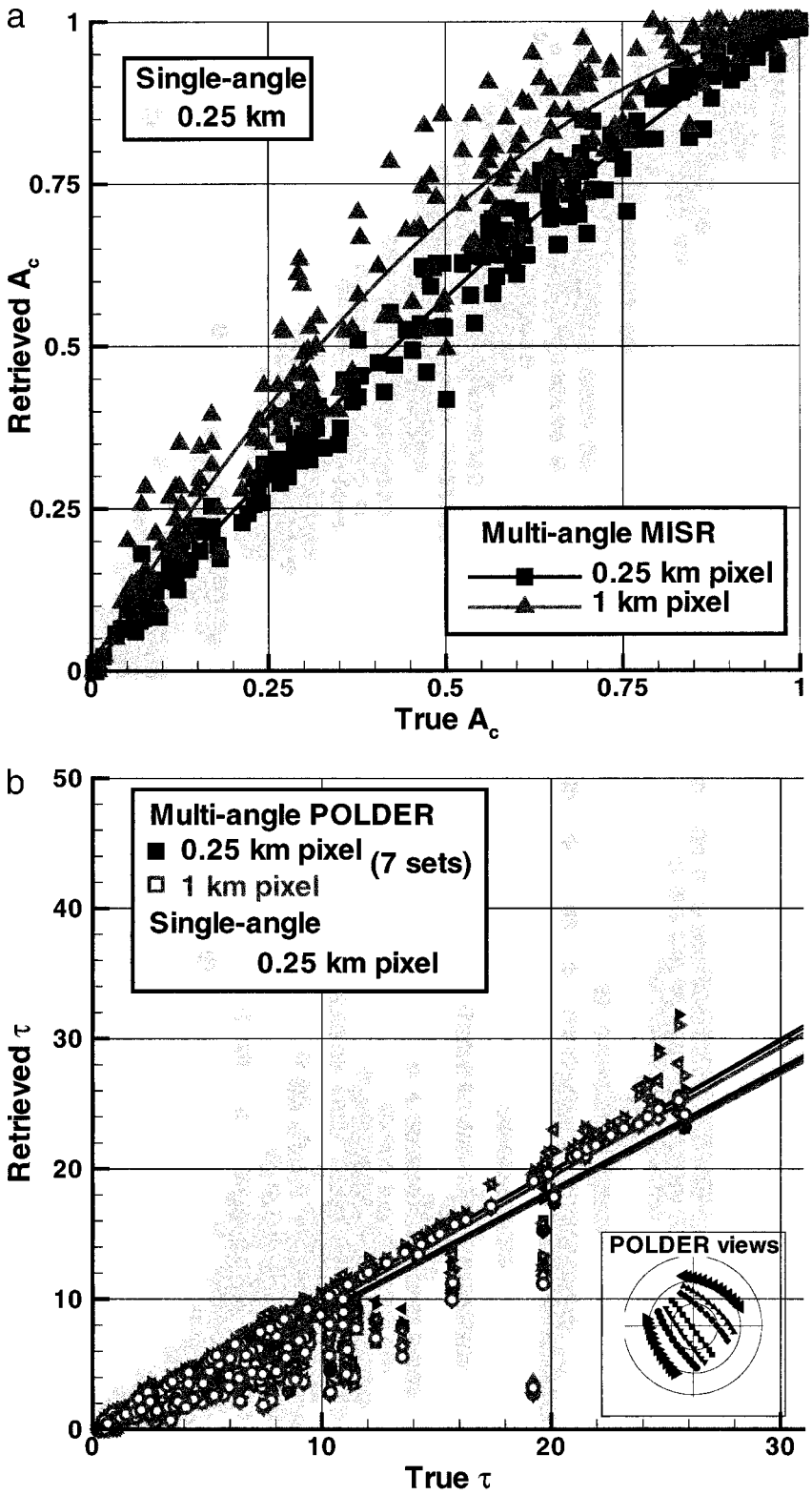

FIG. 3. (a) Retrieved cloud fraction using multiview scene ID from nine MISR angles as compared with single-view method. (b) Retrieved cloud optical depth using multiview scene ID from seven representative sets of POLDER view angles (heavy symbols) as compared with single-angle retrieval (light gray symbols). The POLDER angle sets for seven different days are shown in the inset, which is a polar plot in view angle space. Circles are 30° increments of view zenith angle; backscatter angles are on the left.

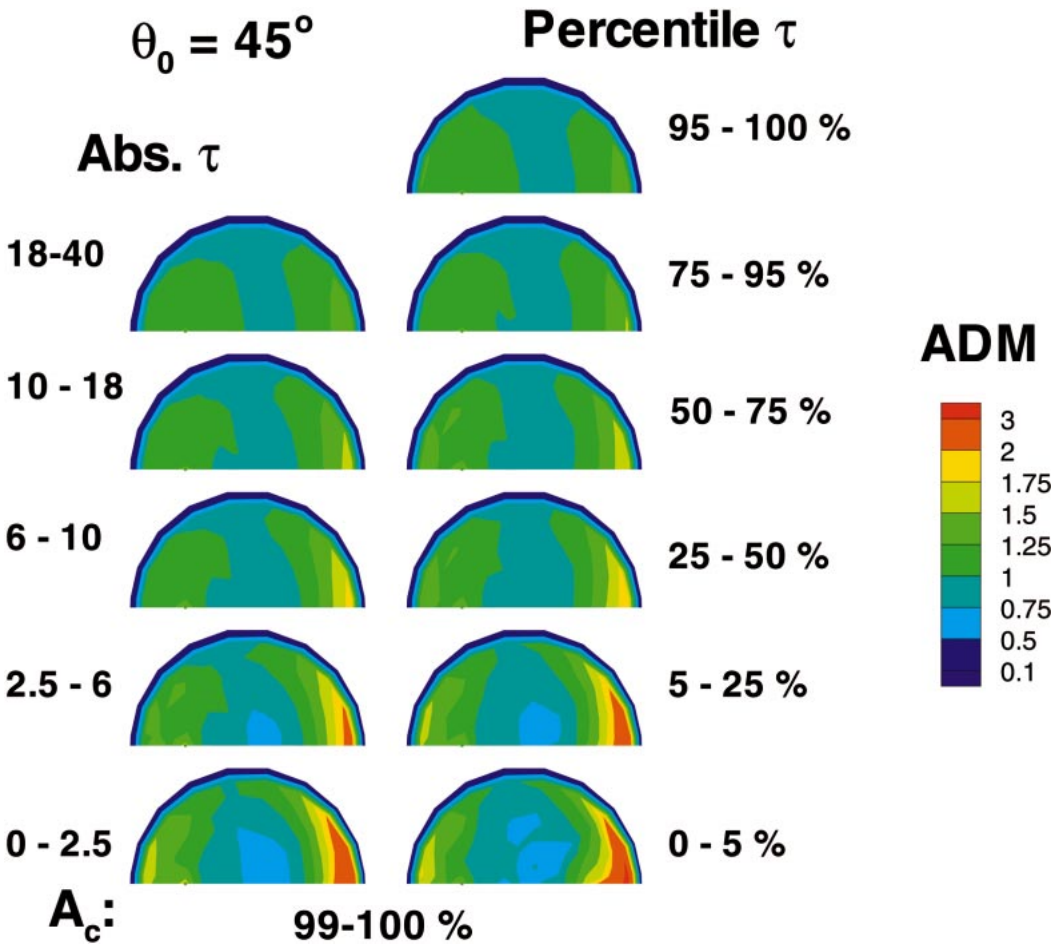

FIG. 4. Sample ADMs built using 1-km pixel-scale imager radiances at 45° sun (overcast clouds only; optical depth increases from bottom to top). Left column is ADMs built from scene ID using absolute optical-depth retrieval. Right column is ADMs built using percentile optical-depth retrieval. View zeniths beyond 70° are not included because of A_c retrieval artifacts.

back. Figure 3a shows the effect on retrieved cloud fraction for the 341 sample scenes in this study when all nine MISR views are combined to obtain a single retrieved cloud fraction. Simple averaging of these nine view angles has no effect on the retrieved mean value, shown by the lines, but reduces the variability of retrieved values considerably.

The multiviewing POLDER instrument (Deschamps 1994) observed the earth recently from the *Advanced Earth Observation Satellite.* This instrument uses a wide-angle lens and charge-coupled device sensor to obtain views of the same region on the earth at up to 14 different view angles per orbital pass. Retrieval of a multiview cloud fraction from these POLDER view angles—but at the 0.25–1-km MODIS scale and not the instrument's actual ~6-km scale—gives very similar results to those found with MISR. Figure 3b shows the effect on the retrieval of optical depth for seven representative sets of POLDER multiple views. Again a substantial reduction in the variability of the retrieval is achieved. In this case, the mean lines cluster about two different values: most of the POLDER view-angle sets, as well as the single-angle retrievals, have a slope of about 93%, so the mean retrieved optical depth is about 7% low. However, as shown in larger symbols in the inset, there are two POLDER view-angle sets that follow almost exactly along a 60°-view zenith angle curve. For both these angle sets, the mean retrieved cloud optical depth is almost exact. The MISR result (not shown) also falls closer to the 1:1 line.

To represent the multiple-view advantage in this study, the scene ID obtained at nadir view will be used. The mean and variability of retrieved cloud fraction for nadir view is almost exactly the same as that shown in Fig. 3a, and the optical depth retrieved at nadir view very closely approximates most of the POLDER angle sets.

e. Step 3: ADM construction

The imager-scale radiances are collected according to the scene ID obtained in step 2 to build ADMs. The meth-

TABLE 2. Cloud fraction and percentile optical depth intervals, with number of true samples.

Cloud fraction interval (%)	Cloud optical depth percentile interval (%)	No. of samples (true scene ID)
0–1	All	20
1–25	0–50	24
	50–100	26
25–50	0–50	24
	50–100	27
50–75	0–33.3	17
	33.3–66.6	20
	66.6–100	20
75–99	0–20	14
	20–40	15
	40–60	15
	60–80	15
	80–100	17
99–100	0–5	3
	5–25	17
	25–50	22
	50–75	22
	75–95	17
	95–100	6

od of sorting by angular bins is used (Green and Hinton 1996; Loeb et al. 1999). The ADM is defined as

$$\psi(\theta, \phi, \theta_0) = \frac{\pi \bar{I}(\theta, \phi, \theta_0)}{\bar{F}_{\text{up}}(\theta_0)}, \quad (6)$$

where $\bar{I}$ is the mean radiance of the scene class and $\bar{F}_{\text{up}}$ is the upward flux computed by integrating the mean radiance over all angles. The ADM empirically captures the nonisotropic behavior of the radiance for a given retrieved scene type. Figure 4 shows some sample ADMs from this process, using 1-km imager-scale radiances, for both absolute and percentile τ scene IDs. These ADMs, based on the scene ID retrieved at each angle, are limited to view zenith angles less than 70°, because, beyond that point, artifacts in retrieval of cloud fraction from the imager become excessive. The ADMs are built consistently, however, such that all energy is accounted for in comparing with the true flux. Of note in both approaches is the strong trend toward Lambertian behavior ($\psi = 1$) with increasing optical depth. In the ERBE processing, all of the ADMs shown in this figure were reduced to a single ADM for overcast scenes [although the scene ID was done differently in ERBE, such that *thin* overcast clouds were often not classified as overcast (Wielicki and Green 1989) but rather as mostly or partly cloudy].

f. Step 4a: Compute flux from ADM

The final step is to apply the ADM to the simulated radiance to obtain a flux. The ADMs are applied as they are in ERBE/CERES practice: the ADM built in step 3 for the scene ID retrieved in step 2 is used to invert the radiance at each angle into a hemispherical flux as

$$F_{\text{retr}}(\theta, \phi, \theta_0) = \frac{\pi I_i(\theta, \phi, \theta_0)}{\psi_I(\theta, \phi, \theta_0)}, \quad (7)$$

where I_i is the radiance of an individual cloud scene and ψ_I is the ADM for that scene type. Note that the retrieved flux is written here as dependent on the viewing zenith and azimuth angles, because in this process different values will be obtained for different view angles because of various error sources in the retrieval process, as discussed in the next section. Here, F_{retr} then can be compared to the true flux, which is known from the SHDOM solution (see section 4b on error distributions).

g. Step 4b: Compute flux from table lookup

A plane-parallel model is used to retrieve flux from the CERES and ISCCP cloud properties for comparison.

4. Results

a. Representativeness of cloud scenes

Results were first generated for comparison with the findings of Loeb and Davies (1996) regarding the dependence of retrieved τ on solar zenith angle and Loeb and Coakley (1998) regarding a view-angle dependence of retrieved τ. The capped model did not reproduce their findings of biased retrievals with view and solar geometry (Figs. 5 and 6). The bumpy model captured the

TABLE 3. Flux bias error (and standard deviation) for latitude zones with *Terra* satellite sampling (%) using absolute and percentile τ scene ID.

		$F_{\text{retr}} - F_{\text{true}}$			
		RAPS		FAPS	
		Jan	Jul	Jan	Jul
Absolute τ	75°–76°N	NS	−3.98 (7.66)	NS	2.83 (5.00)
	60°–61°N	−5.92 (9.18)	0.22 (1.44)	−2.70 (7.58)	−0.25 (1.48)
	30°–31°N	−0.34 (2.93)	2.82 (3.88)	−0.42 (3.20)	2.96 (4.85)
	0°–1°N	2.09 (3.31)	1.86 (3.01)	2.22 (3.76)	1.68 (3.32)
Percentile τ	75°–76°N	NS	−0.59 (1.83)	NS	−1.45 (4.93)
	60°–61°N	−0.12 (2.11)	0.46 (1.12)	−0.77 (3.87)	0.26 (2.55)
	30°–31°N	−0.04 (1.27)	0.72 (2.21)	−0.18 (1.87)	2.18 (4.41)
	0°–1°N	0.80 (1.47)	0.77 (1.60)	1.74 (3.37)	1.49 (2.59)

TABLE 4. Same as Table 3, but for *TRMM* satellite.

	Initial equator crossing time:	$F_{retr} - F_{true}$ RAPS Jan 1200	RAPS Jan 1800	RAPS Jul 1200	RAPS Jul 1800	FAPS Jan 1200	FAPS Jan 1800	FAPS Jul 1200	FAPS Jul 1800
Absolute τ	30°–31°N	−0.51 (6.32)	−3.32 (6.33)	0.91 (3.05)	0.78 (2.98)	2.89 (6.79)	−0.90 (4.20)	0.60 (1.73)	0.71 (1.82)
	0°–1°N	0.59 (3.36)	0.51 (3.36)	0.89 (3.46)	1.27 (4.02)	0.98 (3.55)	1.18 (3.23)	2.02 (2.97)	2.14 (3.80)
Percentile τ	30°–31°N	0.15 (1.67)	−0.70 (1.74)	−0.05 (0.97)	−0.13 (0.92)	−0.25 (2.92)	−2.09 (2.12)	−0.91 (1.96)	−0.88 (1.78)
	0°–1°N	−0.01 (1.13)	−0.07 (1.04)	0.05 (1.28)	0.16 (1.43)	0.13 (1.17)	0.04 (1.15)	−0.14 (1.83)	0.02 (1.57)

solar zenith angle dependence very well (see Fig. 5). The bumpy model also agreed with their findings as a function of view angle except at near-nadir views (view angle $< 30°$) as shown in Fig. 6. This result suggests that the capped model does not describe adequately the actual cloud-top structure of these marine boundary layer cloud fields. The remainder of this paper will, therefore, concentrate on the bumpy model for cloud-top variability (80% of thickness variability in cloud top, leading to cloud-top bumps with $\tau > 1$).

b. Error distributions

Figure 7 shows the angular distribution of flux errors incurred in obtaining flux from satellite-measured radiance, using the process described in section 3, for a 45° solar zenith angle. Figure 7a is for the case with absolute cloud optical-depth classes in the scene ID. Retrieving a scene ID including errors as shown in Figure 2 redistributes the cloud samples in the scene ID space, so that the cloud classes for which results are obtained do not correspond completely to the input classes shown in Table 1. For example, the input cloud samples include 20 cases with 1%–25% cloud fraction and mean optical depth between 2.5 and 6 (Table 1); yet Fig. 7a shows *no* retrieved scenes with this cloud type. Scene ID errors also result in some very systematic error patterns, particularly for the broken cloud fields, with large positive biases in the backscatter direction and negative biases in the forward-scatter direction.

Figure 7b shows similar flux error distributions but using the alternate, percentile optical-depth classes from step 2b. The comparison between Figs. 7a and 7b is not exact, because the scene classes are defined differently in the percentile approach. However, it is apparent that the percentile scene ID approach corrects for some of the systematic errors in retrieved flux that are evident in Fig. 7a.

Figure 7c shows a similar result with the percentile optical depth approach but now using the nadir scene ID to approximate the advantage of multiple views. A significant decrease in the flux bias error is obtained relative to the single-view percentile scene ID.

To assess the validity of the percentile assumption, the calculations in Fig. 7b are repeated using true, not retrieved, cloud fraction. The remaining errors, shown in Fig. 7d, are due to the nonmonotonicity of reflectance at each angle. Cloud-top bumps can make clouds look bright in backscatter but dark (shadowed) in forward scatter. The error associated with the percentile assumption is important (>5%) only for view zenith angles greater than 65° with broken cloudiness. It never exceeds 20%. This shows that, given an accurate cloud fraction, the percentile approach very effectively removes errors due to optical-depth retrieval biases (knowledge of the true cloud fraction also improves the fixed τ approach but does not suffice to bring the bias

TABLE 5. Same as Table 3, but nadir ID approximates multiview ID.

		$F_{retr} - F_{true}$			
		RAPS		FAPS	
		Jan	Jul	Jan	Jul
Absolute τ	75°–76°N	NS	0.50 (3.63)	NS	0.63 (6.00)
	60°–61°N	1.00 (6.94)	0.11 (1.37)	0.71 (6.51)	−0.19 (2.63)
	30°–31°N	0.06 (1.53)	0.15 (1.22)	−0.03 (2.30)	0.37 (2.64)
	0°–1°N	0.03 (0.90)	0.06 (0.94)	0.27 (1.91)	0.18 (1.60)
Percentile τ	75°–76°N	NS	0.02 (3.53)	NS	0.10 (6.67)
	60°–61°N	0.04 (6.22)	0.02 (1.54)	0.08 (7.63)	0.05 (3.40)
	30°–31°N	0.004 (1.74)	0.02 (1.80)	0.05 (2.98)	0.04 (3.67)
	0°–1°N	0.004 (1.22)	−0.01 (1.30)	−0.002 (2.45)	0.05 (2.04)

error to zero because of remaining systematic optical-depth retrieval biases).

c. Instrument/satellite sampling analysis

The flux error distributions shown in the previous section give a complete picture for all view angles. Satellites in Earth orbit have limited viewing opportunities, however, and may scan a particular part of view-angle space repeatedly while rarely or never sampling another portion of that space. In particular, the sampling may be very different near the equator than it is at higher latitudes. The effective flux error in satellite retrievals, therefore, must be obtained as a weighted average of the flux error sampled in view-angle space:

$$\Delta F(\theta_{0k}) = \sum_{\theta_i} \sum_{\phi_j} W_{ijk} \Delta F(\theta_i, \phi_j, \theta_{0k}), \qquad (8)$$

where i is the view zenith angle index, j is the relative azimuth index, and k is the index for the solar zenith angle.

In this study, the view zenith angle for satellite sampling is limited in range to $0° \le \theta \le 70°$. This is the limit beyond which scene ID is not retrieved because of increasing artifacts (see Fig. 2). In application to CERES, this limit applies to the scene ID obtained at MODIS or VIRS imager viewing conditions (actually, VIRS has a 45° view zenith angle limit), not to the CERES viewing zenith itself. Modeling these two different instrument angles is, however, beyond the scope of this simulation. The actual errors incurred on CERES will, therefore, be somewhere between those in Tables 3–4 and those in Tables 5–6, because of the combination of these two different angles.

The weights W_{ijk} are a function both of satellite sampling frequency S_{ijk} and of the size of the field of view, A_{FOV}. The latter can be obtained as a function of satellite viewing angle from a geometric analysis. The combined weights are normalized as

$$W_{ijk} = \frac{S_{ijk} A_{FOV_i}}{\sum_i \sum_j S_{ijk} A_{FOV_i}} \qquad (9)$$

The satellite sampling S_{ijk} is simply the number of times a satellite in a particular orbit views a region of the earth with a particular set of view and solar zenith angles. It has been computed for the *TRMM* and *Terra* satellites, on which the CERES instruments fly, for summer and winter months and for two operating modes: the fixed-azimuth plane scan (FAPS) mode in which the instrument scans in elevation perpendicular to the ground track; and the rotating-azimuth plane scan (RAPS) mode in which the instrument azimuth changes continuously between 90° and 270° while it scans in elevation. The FAPS mode is designed to obtain global geographic coverage. The RAPS mode, because of its greater angular sampling, is intended for building ADMs. The *TRMM* and *Terra* satellites are in very different orbits and are representative of satellites in precessing and sun-synchronous orbits, respectively. In the current study, satellite sampling statistics are accumulated in four latitude bands: 0°–1°N, 30°–31°N, 60°–61°N, and 75°–

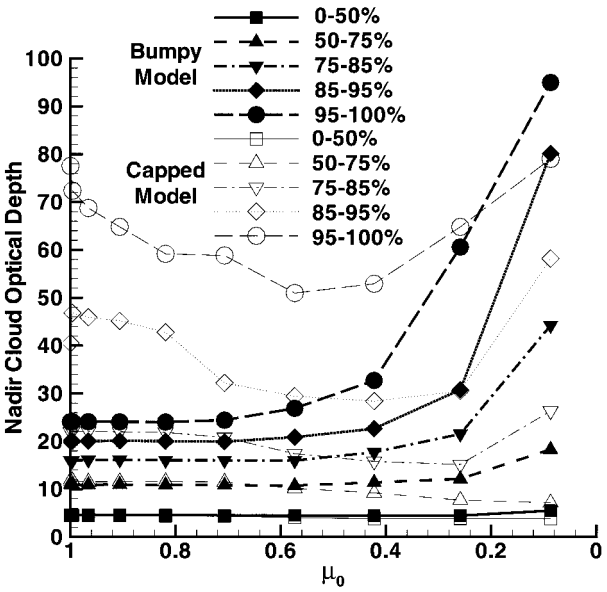

FIG. 5. Retrieved nadir cloud optical depth for overcast clouds in various thickness percentiles of occurrence as a function of solar zenith angle (cf. Fig. 11b of Loeb and Davies 1996).

TABLE 6. Same as Table 4, but nadir ID approximates multiview ID.

		$F_{retr} - F_{true}$									
		RAPS				FAPS					
		Jan		Jul		Jan		Jul			
	Initial equator crossing time:	1200	1800	1200	1800	1200	1800	1200	1800		
Absolute τ	30°–31°N	0.45 (3.01)	0.16 (2.25)	0.17 (1.35)	0.16 (1.30)	0.59 (3.69)	0.23 (2.35)	−0.02 (2.05)	−0.03 (1.91)		
	0°–1°N	0.22 (1.72)	0.19 (1.66)	0.25 (1.84)	0.29 (1.98)	0.23 (1.59)	0.14 (1.61)	0.06 (2.07)	0.15 (1.94)		
Percentile τ	30°–31°N	0.01 (2.71)	0.02 (2.79)	0.01 (1.32)	0.01 (1.31)	0.01 (3.92)	0.01 (2.93)	0.02 (2.50)	0.01 (2.29)		
	0°–1°N	0.01 (1.67)	0.01 (1.67)	0.01 (1.73)	0.01 (1.84)	0.01 (1.48)	0.02 (1.84)	0.04 (2.66)	0.04 (2.39)		

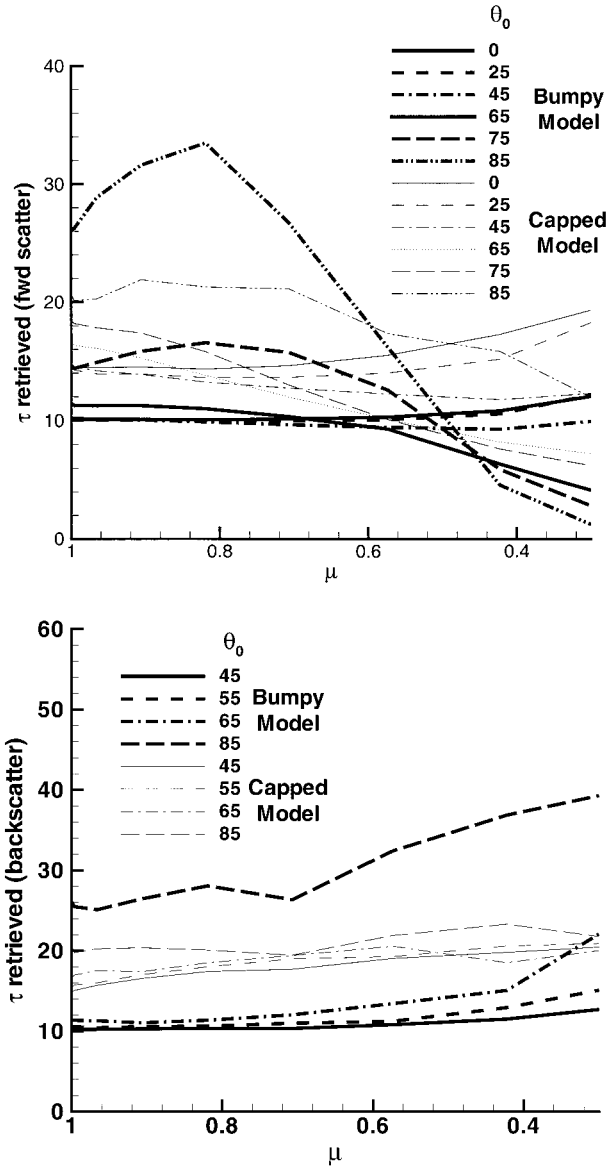

FIG. 6. Retrieved nadir cloud optical depth for overcast clouds at a range of solar zenith angle as a function of view angle (cf. Fig. 13 of Loeb and Coakley 1998).

76°N. To assess errors that include the satellite sampling effect, each cloud field in this study is successively assumed to cover the entire globe. That is, the error statistics that follow are for an earth covered with a variety of marine boundary layer clouds. Therefore, the analysis illuminates errors from view and sun angle, not from tropical versus Arctic cloud types.

Figure 8 gives the sampling pattern for the *Terra* spacecraft in FAPS mode in July. The accompanying statistics on retrieved flux bias errors (Table 7) are for scattered, broken, and overcast cloud classes, using the percentile scene ID. Entry NS denotes no sampling in that particular latitude band for that sampling pattern. ''NS $<$ 70'' means there were no samples with view

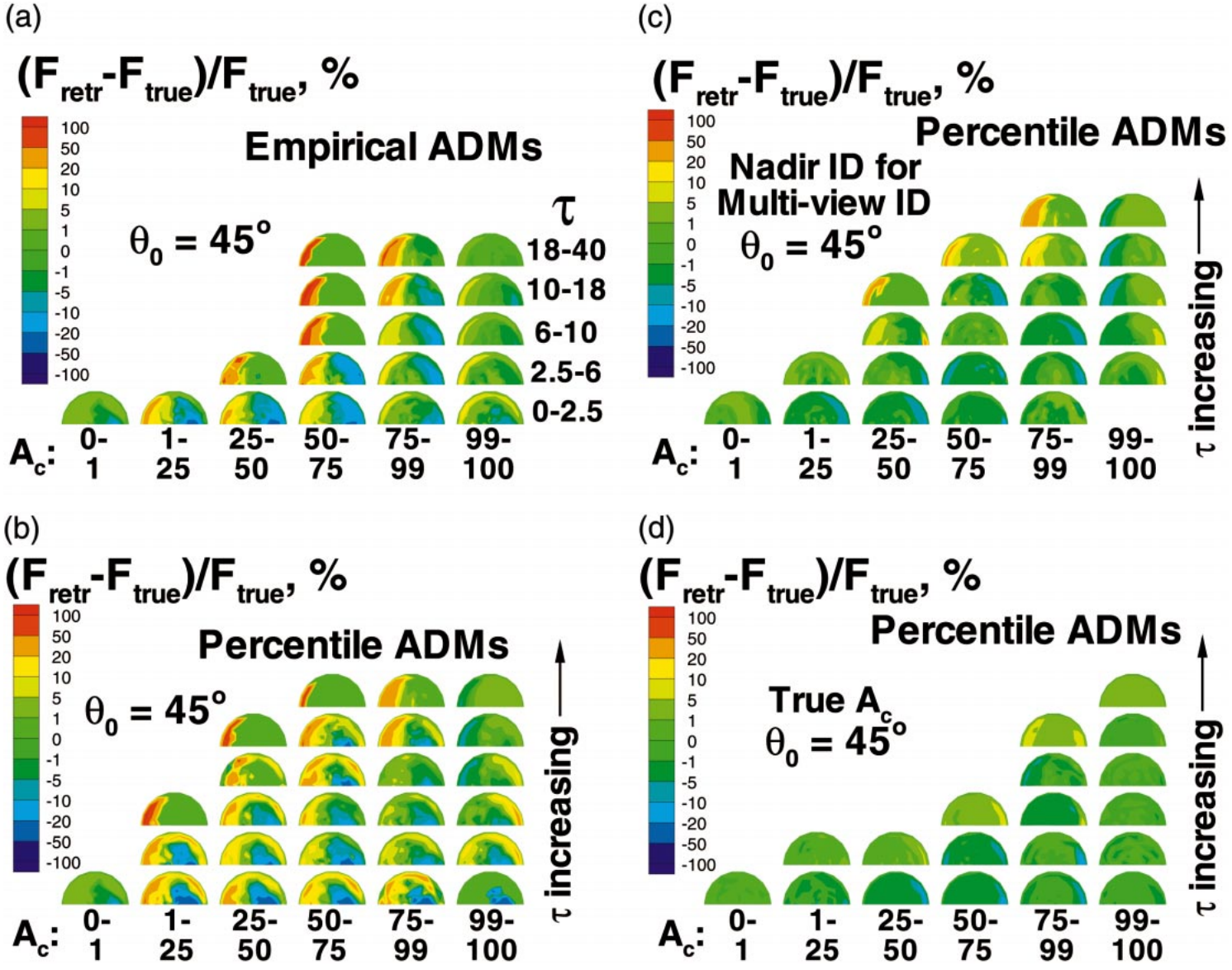

FIG. 7. Flux error distributions at 45° solar zenith angle resulting from (a) the empirical ADM approach with absolute τ, (b) the percentile ADM approach (refer to Table 2 for bin limits), (c) the percentile ADM approach using nadir view to approximate multiple views, and (d) the percentile ADM approach using the true cloud fraction.

TABLE 7. Bias error in retrieved flux (%) corresponding to Fig. 8 for scattered (0%–40% cloud, top of three rows), broken (40%–99% cloud; middle of three rows), and overcast (99%–100% cloud; bottom of three rows) cloud samples in different latitude bands for different solar zenith angles. No sampling is denoted by NS.

	0°	5°	15°	25°	35°	45°	55°	65°	75°	85°	Zonal average	
75°–76°N							−5.3	−6.7	−6.7	7.9	−5.0	All:
	NS	NS	NS	NS	NS	NS	−1.6	−2.5	−1.5	7.2	−1.4	−1.4
							−1.1	1.0	−2.1	−1.7	−0.9	
60°–61°N					−5.3	8.2	NS	NS	−2.4	−2.6	−2.0	All:
	NS	NS	NS	NS	−2.0	4.6	<	<	−2.9	1.6	−0.1	0.36
					0.9	0.3	70°	70°	4.3	2.9	0.9	
30°–31°N	1.7	1.5	−4.1	12.	26.	NS					6.2	All:
	2.5	1.6	−2.7	7.5	16.	<	NS	NS	NS	NS	4.0	2.8
	−0.3	0.02	−0.3	0.4	−1.0	70°					0.1	
0°–1°N			−3.3	−8.0	7.6	30.					2.9	All:
	NS	NS	−0.4	−3.2	5.2	15.	NS	NS	NS	NS	2.6	1.5
			0.1	0.5	0.2	−1.7					0.3	

zenith angle less than 70°, the cutoff for retrieval of scene ID. Figure 9 and Table 8 are the corresponding information for RAPS mode. RAPS has much better coverage in view angle space, but, of course, both modes sample the same solar zenith angle space. Of note in both figures is the cancellation of errors that occurs between different solar zenith angles. The cancellation of large errors of opposing sign in the different solar zenith angle bins results in perhaps deceptively small zonal average errors. This effect should be kept in mind while examining the results of the next section. Also of interest is the tendency to a more consistent underestimate of flux for sampling patterns characteristic of higher latitudes. When generating zonal profiles from satellite data to compare with models, this bias may be important.

1) ZONAL AVERAGE FLUX ERROR—SINGLE VIEW

Tables 3 and 4 summarize the overall flux errors averaged over all cloud samples in this study in each latitude zone, weighted by sampling frequency for *Terra* and *TRMM* (not diurnally averaged) and using both absolute and percentile scene ID. Retrievals for view zenith angles beyond 70° are not included, because of increasing artifacts in the scene ID at such angles. Again, NS denotes no sampling and occurs for *Terra* because the sun never tops the horizon in winter at high

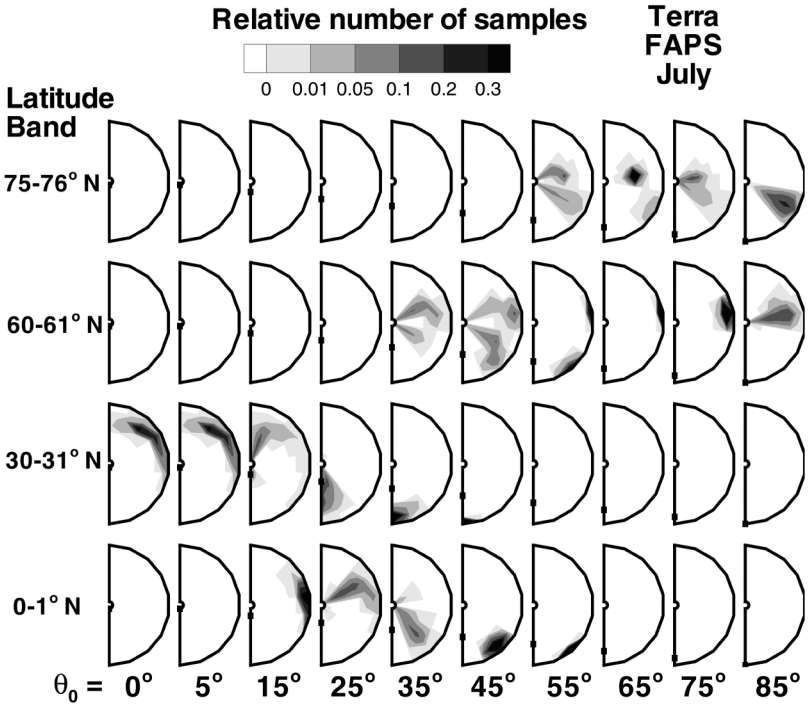

FIG. 8. *Terra* orbital sampling patterns for Jul in FAPS mode. Dots denote the position of the sun in the view angle space.

TABLE 8. Same as Table 7, but corresponding to Fig. 9.

	0°	5°	15°	25°	35°	45°	55°	65°	75°	85°	Zonal average	
75°–76°N							−2.6	−1.8	−2.1	5.6	−1.7	All:
	NS	NS	NS	NS	NS	NS	−1.1	−1.5	−0.2	5.4	−0.7	−0.6
							−0.5	0.9	−0.9	0.3	−0.3	
60°–61°N					−1.8	5.5	NS	NS	0.2	−0.9	0.2	All:
	NS	NS	NS	NS	−0.5	3.8	<	<	−2.5	0.1	0.7	0.5
					0.3	−0.3	70°	70°	5.8	1.7	0.2	
30°–31°N	2.6	1.7	−4.7	8.5	26.	NS					1.9	All:
	2.4	1.8	−2.4	5.3	15.	<	NS	NS	NS	NS	1.5	0.7
	−0.6	−0.5	−0.3	0.2	−0.9	70°					−0.1	
0°–1°N			NS	−3.2	3.6	27.					1.3	All:
	NS	NS	<	−1.6	3.1	15.	NS	NS	NS	NS	1.4	0.8
			70°	0.1	0.2	−1.9					0.2	

latitude. Bias errors generally go from positive to negative and the standard deviation of the error generally increases as the zone of interest increases in latitude, which again has implications for zonal-average flux profiles derived from satellite data.

Note that *TRMM*, Table 4, in an orbit inclined at 35°, does not ever see the two northernmost latitude bands. As a precessing spacecraft, the sampling on *TRMM* also depends on where the spacecraft is in its precession. Cases are considered for which the equator crossing time at the beginning of the month is either 1200 or 1800. As a rule, the equator crossing time has only a small effect on the amount of error incurred, except in January, near the northernmost part of the orbit.

All these results are for 1-km imager pixels. Errors for 0.25-km imager pixels are not shown but range from the same order of magnitude to about one-half of those reported in the following tables and lead to similar conclusions.

For both satellites, the percentile approach offers a noticeable error reduction, especially for the standard deviation (or variability) of the flux error. Flux bias errors in the percentile approach are considerably smaller for both satellites, with few exceptions. Even in these cases, the bias errors are still small in an absolute sense. In several sampling conditions, the flux bias error is very near zero. However, in examining the details as a function of sun angle, as shown in Tables 7 and 8, recall that this small error in many cases results from a cancellation of larger errors in each sun-angle bin.

To check the statistical significance of these results, the same ADMs were applied to 130 independent cloud

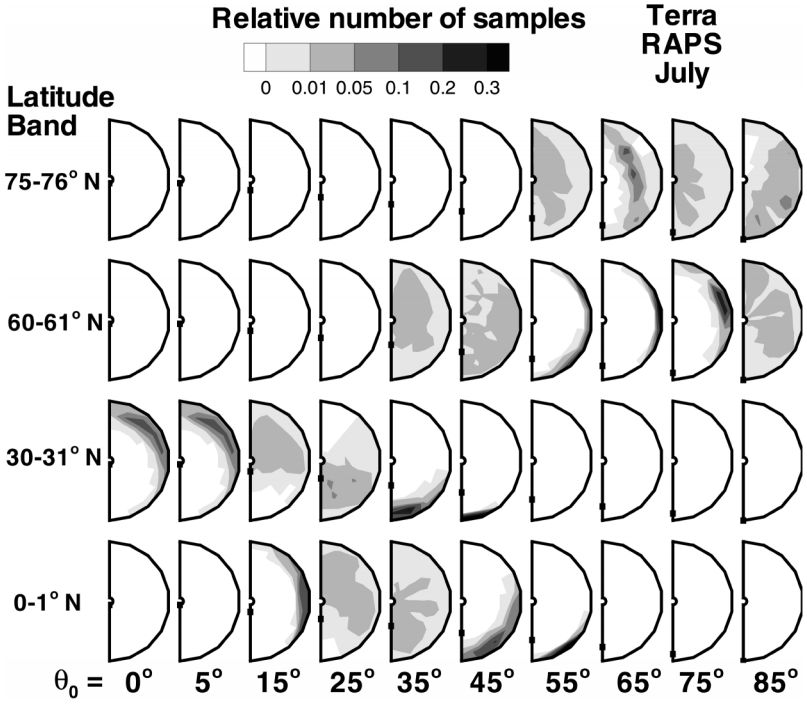

FIG. 9. Same as Fig. 8, but for RAPS mode.

TABLE 9. Same as Table 3, but only for percentile τ scene ID, and using plane-parallel table lookup.

		$F_{retr} - F_{true}$			
		RAPS		FAPS	
		Jan	Jul	Jan	Jul
CERES threshold	75°–76°N	NS	28.0 (11.6)	NS	35.9 (15.7)
	60°–61°N	58.2 (23.8)	17.0 (7.54)	59.1 (23.0)	19.3 (8.02)
	30°–31°N	13.3 (5.93)	11.7 (6.47)	15.0 (6.86)	11.4 (8.20)
	0°–1°N	11.9 (6.10)	12.0 (6.23)	13.2 (7.86)	12.1 (7.23)
ISCCP threshold	75°–76°N	NS	19.9 (8.99)	NS	23.7 (11.2)
	60°–61°N	38.6 (18.1)	13.2 (6.40)	38.1 (18.8)	13.8 (6.69)
	30°–31°N	10.4 (4.90)	11.1 (6.40)	11.3 (5.35)	11.1 (8.11)
	0°–1°N	10.9 (5.93)	11.1 (6.04)	12.3 (7.50)	11.4 (6.89)

field samples subsampled from the same 45 Landsat cloud fields. The results, for both bias and rmse, are very consistent with those in Tables 3 and 4, giving confidence in the robustness of the conclusions drawn in this paper.

2) ZONAL AVERAGE FLUX ERROR—MULTIPLE VIEW

As indicated in section 3, the advantage of multiple views is mainly in reducing the scene ID error. Flux errors obtained using the nadir ID for each scene, which approximates the scene ID improvement from MISR- or POLDER-like multiple views, are summarized in Table 5 (*Terra* orbital sampling) and Table 6 (*TRMM* orbital sampling).

A consistent and significant reduction in the flux bias error is obtained by using a multiview scene ID. The effect on the standard deviation (variability) of the errors is less consistent: it is substantially reduced for the absolute τ approach but generally increases for the percentile τ approach. Because the multiview approach uses a single ID for each scene, it does not really take advantage of the percentile approach, which groups bright and dark pixels, at whatever view angle, together. The trade-off between these two paths to error reduction thus depends on whether it is more desirable to reduce bias errors or variability.

3) ZONAL-AVERAGE FLUX ERROR—PLANE-PARALLEL RETRIEVAL

The simplest approach to retrieving flux is to assume plane-parallel conditions exist and to obtain the flux from the scene ID by table lookup. Table 9 summarizes the flux errors incurred using this approach, for both CERES and ISCCP cloud thresholds, for the *Terra* satellite. *TRMM* results (not shown) are of the same order of magnitude. This simple approach clearly results in an unacceptably large flux bias error. The standard deviation of the error is also considerably larger than for the other approaches.

The trend of increasing errors with latitude is even more dramatic in the plane-parallel case than for the empirical ADM approach but is reduced somewhat when the ISCCP threshold is used.

5. Discussion and conclusions

a. Error sources and attribution

The problem of obtaining hemispherical flux from a satellite-measured radiance has a number of pitfalls, both in the theoretical simulation and in the real processing. These will be discussed individually and, if possible, quantified.

1) DISCRETIZATION

Discretization error occurs by the selection of a finite number of ADMs to invert the cloud scenes. With the coincident imager instruments, CERES is designed to reduce this error by allowing a finer discretization of ADMs based on a variety of scene parameters (200 scene types vs 12 for ERBE; Wielicki et al. 1995b). Discretization error in the theoretical simulation can be estimated from the difference between values of adjacent ADMs. For individual cases, the maximum discretization error is 12%–30%; however this error averages to zero over all the samples used to build the ADMs. Thus, this source contributes only to instantaneous or rms error.

2) BEAM FILLING

Beam filling occurs when a broken cloud within an imager pixel is bright or extensive enough to trigger the cloud reflectance threshold and the pixel is classified as cloudy. This contributes to the error in the scene ID for cloud fraction and thence to an error in mean cloud optical depth. The effect can be examined by looking at the difference in results at various pixel scales. Figure 2a shows a bias in retrieved cloud fraction between 0.25- and 1-km imager pixels on the order of 0.10. Strictly speaking, cloud-mask thresholds should change for different pixel sizes, but this is not yet in the plans for CERES processing (D. F. Young 1999, personal communication) and is not always done. The positive bias

found in this study is due to the contribution of broken and near-overcast cloud fields, for which the imager fails to resolve small spaces between cloud elements. Clouds are missed entirely—resulting in pixels classified as clear—only as the cloud fraction becomes very small. These results are entirely consistent with a previous study of cloud fraction versus imager pixel size (Wielicki et al. 1995b).

3) SCENE ID

The largest source of error is the misidentification of a scene. In this study, that means the misidentification of cloud fraction and/or cloud optical depth. When the true scene ID is used in the inversion processing, the bias error is reduced essentially to zero while the standard deviation drops by a factor of 3–6 (not shown).

4) PLANE-PARALLEL BIAS

This bias is introduced in two ways: retrieval of the scene ID and table lookup of the flux. Figure 2 illustrates the effect on scene ID. Table 9 shows the impact on flux retrieval. Retrieving flux by assuming a plane-parallel pixel and using table-lookup results in unacceptable bias errors. The effect of plane-parallel bias on scene ID, in the context of using empirical ADMs to retrieve flux, results in errors that are much smaller, especially when using the percentile τ approach (Loeb et al. 2000).

5) INTERPOLATION

There are two kinds of interpolation that may cause error. Actual satellite measurements occur at a variety of view angles and must be interpolated to the angular grid of the ADMs. This error source is not addressed here, because all calculations and retrievals are done for the same set of angles as defined in section 2c. The second possible interpolation error is interpolation between angular models based on the actual scene ID (cloud fraction and optical depth) of a sample. Attempts to implement this kind of interpolation did not reduce flux errors. The reason for this may be that such interpolation breaks the complete consistency between how ADMs are built and how they are used, which is required to obtain unbiased results on average. Thus, interpolation is not used in this paper.

b. Implications

This paper reports on a comprehensive study to evaluate errors in shortwave flux retrieved from satellite-measured radiances, in the presence of nonplane-parallel clouds. The study is restricted to single-layer low water clouds over ocean, for which optical-depth distributions are obtained using Landsat scenes. The SHDOM radiative transfer code is used to compute complete radiance fields on 2D (vertical plus one horizontal dimension) extinction fields generated from the Landsat scenes. The simulation is shown first to be reasonably consistent with observed properties of actual cloud fields, indicating that the cloud model has captured important features of nonhomogeneous cloud fields.

Flux errors computed using a number of approaches show the following conclusions.

1) Inversion to flux using a plane-parallel table lookup results in unacceptably large flux bias errors (11%–60% bias error depending on the orbital viewing geometry).
2) Inversion to flux using empirical ADMs with absolute τ retrievals results in a much smaller flux bias error (down to, at most, 6% bias) and about a 50% reduction in rmse.
3) Use of percentile τ for scene identification yields further improvement over absolute τ retrievals in both bias error (reduced by about a factor of 2 overall to no more than 2% bias) and error variability (also reduced about a factor of 2).
4) Scene ID based on multiple view angles such as are provided by the MISR or POLDER instruments results in smaller flux bias errors than single-view retrievals (factor of about 5 reduction in absolute τ approach to no more than 1% bias; factor of 3–10 reduction for percentile τ approach to no more than 0.1% bias). Root-mean-square error decreases for the absolute τ approach but generally increases by about 30%–40% for the percentile τ approach, reflecting the differences in the two methods.
5) Using the percentile τ approach, bias errors in retrieved flux are found to be less than 1% for overcast scenes, between -1.4% and 4% for broken cloud scenes, and between -5% and 6.5% for scattered cloud scenes, depending on the particular set of viewing geometries that are sampled by a satellite.
6) The main contributor to the flux bias error is found to be error in the scene identification, which is used to determine the angular distribution model used for that scene. Thus, improvements in cloud detection and optical depth retrievals are key to reducing these errors.

The study finds a very consistent trend that the flux bias error (retrieved minus true flux) becomes more negative at higher latitudes. This error is due strictly to the fact that solar zenith and effective scattering angles change for satellites at different latitudes, because in this study the same cloud fields are assumed to cover the entire globe. Given the importance of satellite measurements for determining heat transport from equator to pole, this consistent bias should be kept in mind and efforts should be made to reduce it in the future. Future studies can also examine this trend while accounting for the different cloud types in different regions on the earth, using data from new satellite instruments.

Acknowledgments. Discussions with Professor K. Franklin Evans at the University of Colorado and David F. Young of NASA Langley Research Center were very helpful. Three anonymous reviewers provided very helpful comments for content and clarity.

REFERENCES

Austin, P., Y. Wang, R. Pincus, and V. Kujala, 1995: Precipitation in stratocumulus clouds: Observational modeling and results. *J. Atmos. Sci.,* **52,** 2329–2352.

Barkstrom, B. R., 1984: The Earth Radiation Budget Experiment (ERBE). *Bull. Amer. Meteor. Soc.,* **65,** 1170–1185.

Cahalan, R. F., W. Ridgway, W. J. Wiscombe, S. Gollmer, and Harshvardhan, 1994: Independent pixel and Monte Carlo estimates of stratocumulus albedo. *J. Atmos. Sci.,* **51,** 3776–3790.

Chambers, L. H., 1997: Computation of the effects of inhomogeneous clouds on retrieval of remotely sensed properties. Preprints, *Ninth. Conf. on Atmospheric Radiation,* Long Beach, CA, Amer. Meteor. Soc., 378–382.

——, B. A. Wielicki, and K. F. Evans, 1997: Accuracy of the independent pixel approximation for satellite estimates of oceanic boundary layer cloud optical depth. *J. Geophys. Res.,* **102,** 1779–1794.

Considine, G., J. A. Curry, and B. A. Wielicki, 1997: Modeling cloud fraction and horizontal variability in marine boundary layer clouds. *J. Geophys. Res.,* **102,** 13 517–13 525.

Deschamps, P. Y., F.-M. Bréon, M. Leroy, A. Podaire, A. Bricaud, J.-C. Buriez, and G. Sèze, 1994: The POLDER mission: Instrument characteristics and scientific objectives. *IEEE Trans. Geosci. Remote Sens.,* **32,** 598–615.

Diner, D., and Coauthors, 1998: Multiangle Imaging SpectroRadiometer (MISR) description and experiment overview. *IEEE Trans. Geosci. Remote Sens.,* **36,** 1072–1087.

Evans, K. F., 1998: The Spherical Harmonics Discrete Ordinate Method for three-dimensional atmospheric radiative transfer. *J. Atmos. Sci.,* **55,** 429–446.

Green, R. N., and P. O. Hinton, 1996: Estimation of angular distribution models from radiance pairs. *J. Geophys. Res.,* **101,** 16 951–16 959.

Harshvardhan, B. A. Wielicki, and K. M. Ginger, 1994: The interpretation of remotely sensed cloud properties from a model parameterization perspective. *J. Climate,* **7,** 1987–1998.

Loeb, N. G., and R. Davies, 1996: Observational evidence of plane parallel model biases: Apparent dependence of cloud optical depth on solar zenith angle. *J. Geophys. Res.,* **101,** 1621–1634.

——, and J. A. Coakley Jr., 1998: Inference of marine stratus cloud optical depths from satellite measurements: Does 1D theory apply? *J. Climate,* **11,** 215–233.

——, T. Varnai, and D. M. Winker, 1998: Influence of subpixel-scale cloud-top structure on reflectances from overcast stratiform cloud layers. *J. Atmos. Sci.,* **55,** 2960–2973.

——, P. O. Hinton, and R. N. Green, 1999: Top-of-atmosphere albedo estimation from angular distribution models: A comparison between two approaches. *J. Geophys. Res.,* **104,** 31 225–31 260.

——, F. Parol, J.-C. Buriez, and C. Vanbauce, 2000: Top-of-atmosphere albedo estimation from angular distribution models using scene identification from satellite cloud property retrievals. *J. Climate,* **13,** 1269–1285.

Martin, G. M., D. W. Johnson, and A. Spice, 1994: The measurement and parameterization of effective radius of droplets in warm stratocumulus clouds. *J. Atmos. Sci.,* **51,** 1823–1842.

Miles, N. L., J. Verlinde, and E. E. Clothiaux, 2000: Cloud droplet size distributions in low-level stratiform clouds. *J. Atmos. Sci.,* **57,** 295–311.

Minnis, P., P. W. Heck, D. F. Young, C. W. Fairall, and B. J. Snider, 1992: Stratocumulus cloud properties derived from simultaneous satellite and island-based instrumentation during FIRE. *J. Appl. Meteor.,* **31,** 317–339.

Nakajima, T., and M. D. King, 1990: Determination of the optical thickness and effective particle radius of clouds from reflected solar radiation measurements. Part I: Theory. *J. Atmos. Sci.,* **47,** 1878–1893.

Nordeen, M. L., P. Minnis, D. R. Doelling, D. Pethick, and L. Nguyen, 2001: Satellite observations of cloud plumes generated by Nauru. *Geophys. Res. Lett.,* **28,** 631–634.

Priestley, K. J., and Coauthors, 2000: Postlaunch radiometric validation of the Clouds and the Earth's Radiant Energy System (CERES) Proto-Flight Model on the Tropical Rainfall Measuring Mission (TRMM) spacecraft through 1999. *J. Appl. Meteor.,* **39,** 2249–2258.

Rogers, R. R., and M. K. Yau, 1989: *A Short Course in Cloud Physics.* 3d ed. Pergamon Press, 290 pp.

Rossow, W. B., and L. C. Garder, 1993: Cloud detection using satellite measurements of infrared and visible radiances for ISCCP. *J. Climate,* **6,** 2341–2369.

Tsay, S.-C., K. Stamnes, and K. Jayaweera, 1990: Radiative transfer in stratified atmospheres: Development and verification of a unified model. *J. Quant. Spectrosc. Radiat. Transfer,* **43,** 133–148.

Watts, P. D., C. T. Mutlow, A. J. Baran, and A. M. Zavody, 1998: Study on cloud properties derived from Meteosat second generation. Eumetsat ITT Tech. Rep. 97/181, 344 pp.

Wielicki, B. A., and R. M. Welch, 1986: Cumulus cloud properties derived using Landsat satellite data. *J. Climate Appl. Meteor.,* **25,** 261–276.

——, and R. N. Green, 1989: Cloud identification for ERBE radiative flux retrieval. *J. Appl. Meteor.,* **28,** 1133–1146.

——, and L. Parker, 1992: On the determination of cloud cover from satellite sensors: The effect of sensor spatial resolution. *J. Geophys. Res.,* **97,** 12 799–12 823.

——, R. D. Cess, M. D. King, D. A. Randall, and E. F. Harrison, 1995a: Mission to Planet Earth: Role of clouds and radiation in climate. *Bull. Amer. Meteor. Soc.,* **76,** 2125–2153.

——, R. N. Green, C. J. Tolson, and A. Fan, 1995b: Clouds and the Earth's Radiant Energy System (CERES) Algorithm theoretical basis document. Vol. 3—Cloud analyses and determination of improved top of atmosphere fluxes (Subsystem 4). NASA Reference Publ. RP 1376, 259 pp.

Wielicki, B. A., B. R. Barkstrom, E. F. Harrison, R. B. Lee III, G. L. Smith, and J. E. Cooper, 1996: Clouds and the Earth's Radiant Energy System (CERES): An Earth Observing System experiment. *Bull. Amer. Meteor. Soc.,* **77,** 853–868.